3-D FDTD Modeling of Long-Distance VLF Propagation in the Earth-Ionosphere Waveguide

Sean Burns, *Student Member, IEEE*, Forrest Gasdia, Jamesina J. Simpson, *Senior Member, IEEE*, and Robert A. Marshall, *Member, IEEE*

Abstract— Very-low-frequency (VLF) electromagnetic wave propagation is modeled for the first time over 1000 km scale distances using a 3-D finite-difference time-domain (FDTD) model of the Earth-ionosphere waveguide. Specifically, propagation paths of 2000 km in length are studied, with each simulation requiring 28k processing cores and over 45 h of real time and using ~3.9 TB. A variety of propagation scenarios are tested, including daytime and nighttime propagation paths, a realistic ground propagation path extending from the NAA VLF transmitter in Cutler, ME, USA, toward New Mexico, and day-to-night ionospheric transitions. The 3-D FDTD model results are compared with 2-D azimuthally symmetric FDTD and the long-wave propagation capability (LWPC) results to both validate the 3-D model and understand the impact a fully 3-D model can have on the propagation predictions. The results in this article identify under what conditions and also at what propagation distances, a fully 3-D model is most beneficial.

Index Terms— Daytime propagation, Earth-ionosphere waveguide, finite-difference time-domain (FDTD), ionosphere, long-wave propagation capability (LWPC), magnetized plasma, nighttime propagation, surface impedance boundary condition (SIBC), very-low-frequency propagation (VLF).

I. INTRODUCTION

THE Earth-ionosphere waveguide is defined as the spherical cavity between the Earth's surface and the ionosphere. Very-low-frequency (VLF; 3–30 kHz) electromagnetic waves can propagate very long distances with low attenuation rates of just a few decibels per 1000 km in the Earth-ionosphere waveguide [1]. These waves may be generated by natural electrical processes in the atmosphere, such as lightning, and also by man-made antennas [2]. Applications of VLF waves include long-distance communications (e.g. [3]), lightning geolocation (e.g. [4]), monitoring the D-region of the ionosphere (e.g. [5]), and communications with submarines (e.g. [6]).

Until ~2000, the study of VLF propagation in the Earth-ionosphere waveguide was primarily predicted using analytical calculations (e.g. [7], [8]) and numerical solutions e.g. [9], [10] based on waveguide mode theory. For example, during the 1970's and 1980's, the Naval Oceans System Center developed a software called the long-wavelength propagation capability (LWPC) for modeling propagation from VLF transmitters. LWPC is based on the 2-D waveguide mode theory of [7], which accounts for the ionosphere's D-region electron density profile, the Earth's magnetic field, and the curvature of the Earth. LWPC divides the propagation path into discrete segments, which means the geometry of the problem and the electromagnetic fields do not change perpendicular to the direction of propagation. LWPC is fast and not computationally intensive. For example, solutions for a 2000 km propagation path are typically obtained today within 10 s.

Since about the year 2000, improved computing capabilities have provided the means of generating 2-D, grid-based models of VLF propagation based on the finite-element method (FEM) [11] and the finite-difference time-domain (FDTD) [12], [13] method [14]–[18]. FDTD allows for modeling of more complex geometries, but it is more computationally demanding than LWPC and requires longer run times. For example, solutions for a 2000 km propagation path may be obtained within 6 h using C++ with OpenMP on a 12 core processor.

In this article, VLF propagation is modeled for the first time over 1000 km-scale distances using a 3-D, grid-based algorithm. VLF propagation over shorter (on the order of 200 km) distances was previously modeled in a regional FDTD grid in [19] and [20]. Here a regional 3-D FDTD model of the Earth-ionosphere waveguide is developed by extracting a 3-D region of the global model initially developed in [21], and advanced to permit higher resolutions in [22] and accommodation of ionospheric magnetized plasma in [23]. Several propagation scenarios are tested, including daytime and nighttime propagation paths, a realistic ground propagation path, and daytime-to-nighttime ionospheric transitions.

Section II introduces the regional 3-D FDTD Earth-ionosphere waveguide model and provides descriptions of the ionospheric plasma algorithm, surface impedance boundary condition used at the Earth's surface, and the absorbing boundary condition used on the top side of the grid. Section III describes how the 2000 km propagation path is modeled, how the dispersion errors are corrected, and provides a summary
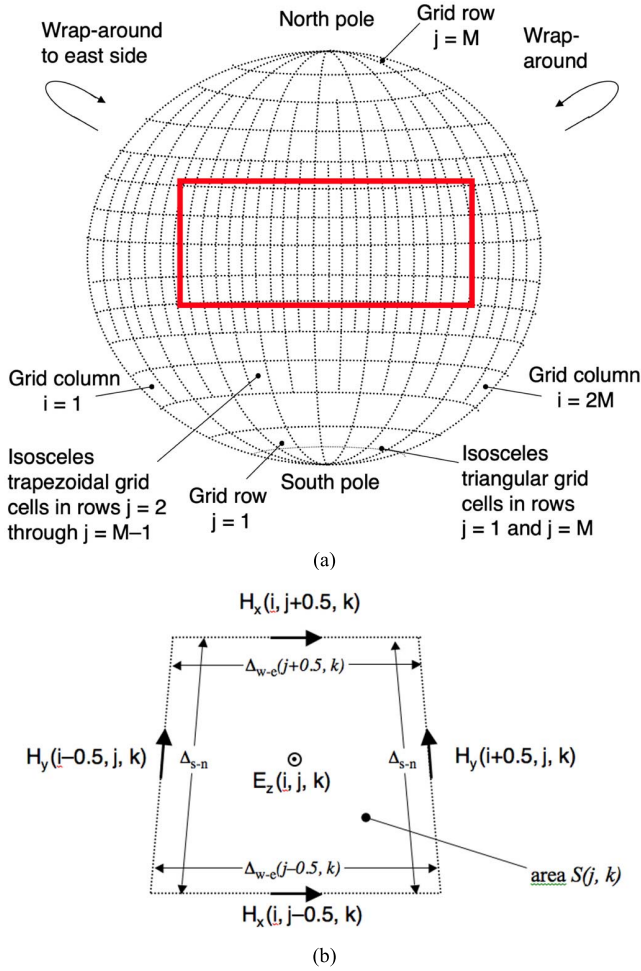
Fig. 1. (a) 2-D slice along the surface of the Earth of the global 3-D FDTD model (not drawn to scale). The red box highlights where the regional 3-D FDTD model is located. Note that any propagation path of interest may be modeled using the regional grid by appropriately setting the ground and ionospheric conditions to the actual path of interest. Figure adapted from [21]. (b) Example of horizontal slice of a trapezoidal grid cell comprising the regional grid.

of the computational requirements. Section IV describes the details of the LWPC and 2-D azimuthally symmetric FDTD models used for comparison with the 3-D FDTD results. Section V presents the results and comparisons between the models for the various propagation paths. Finally, Section VI provides the conclusion.

II. REGIONAL 3-D FDTD EARTH-IONOSPHERE WAVEGUIDE MODEL

Fig. 1(a) shows a 2-D slice of the 3-D global FDTD model of [21] at the surface of the Earth. For simplicity, the regional model is centered at the equator as indicated by the red box shown in Fig. 1(a). Furthermore, the propagation path of interest in the regional model is aligned with the equator. By aligning the regional model with the equator of the global model, the grid arrangement of the regional model is kept as simple as possible (it avoids the polar regions and the merging of cells in west–east (w–e) direction as either pole is approached, for example). Note that any propagation path of interest may be modeled in the regional grid by appropriately

setting the ground and ionospheric conditions to the actual path of interest.

Ampere's and Faraday's laws in their integral forms are applied to implement leapfrog time stepping relations for the electric (E) and magnetic (H) field vector components within the trapezoidal cells of the regional grid. For example, Ampere's law in integral form is applied to develop an FDTD time stepping relation for the electric field at the center of the (i, j, k)th trapezoidal grid cell. For example, referring to Fig. 1(b), we have

$$
E_z^{n+1}(i, j, k) = E_z^n(i, j, k) + \frac{\Delta t}{\epsilon_0 S(j, k)}
$$
$$
\times \left\{ H_x^{n+0.5}(i, j - 0.5, k) \Delta_{w-e}(j - 0.5, k) \right.
$$
$$
- H_x^{n+0.5}(i, j + 0.5, k) \Delta_{w-e}(j + 0.5, k)
$$
$$
+ \left[\begin{array}{c} H_y^{n+0.5}(i + 0.5, j, k) - \\ H_y^{n+0.5}(i - 0.5, j, k) \end{array} \right] \Delta_{s-n} \right\}
$$
$$
- \frac{\Delta t}{\epsilon_0} J_z^{n+0.5}(i, j, k) \tag{1}
$$

where Δt is the time step increment, ε_0 is the permittivity of free space, n is the time step number, J is the current density (which is nonzero only at the VLF source and within the magnetized ionosphere, see Section II-A), Δ_{s-n} is the spatial grid cell dimension in the south–north $(s - n)$ direction, and $S(j, k)$ is the area of the trapezoidal grid cell face.

$$
S(j, k) = \left[\Delta_{w-e}(j - 0.5, k) + \Delta_{w-e}(j + 0.5, k) \right] \frac{\Delta_{s-n}}{2}. \tag{2}
$$

The spatial grid cell dimensions in the w–e directions are

$$
\Delta_{w-e}(j + 0.5, k) = R \Delta\phi \sin\left[(M - j) \frac{\pi}{M} \right]
$$
$$
\Delta_{w-e}(j - 0.5, k) = R \Delta\phi \sin\left[(M - j + 1) \frac{\pi}{M} \right] \tag{3}
$$

where M is the total number of grid cells in the s–n direction of the corresponding full global model and R is the radius from the center of the Earth to the altitude of the grid cell.

All the other electric and magnetic field components in the trapezoidal cells of the regional model are updated in an analogous manner, see [21].

A. Magnetized Ionospheric Plasma Algorithm

The magnetized plasma model of [23] is used to account for the magnetized ionospheric plasma. Compared to other approaches (e.g. [24], [25]), this plasma algorithm avoids costly matrix inversions during time stepping, and it also permits singular updates to the current density equation when a time stepping increment required for the current density equation (Δt_c) is smaller than the time stepping increment required for Maxwell's equations (Δt). This occurs at low altitudes in the Earth-ionosphere waveguide.

All three Cartesian components of the current density, J, in the magnetized plasma are colocated with the vertical (radial) electric field component. They are updated

as follows:

$$\begin{bmatrix} J_x \\ J_y \\ J_z \end{bmatrix}^{n+\frac{1}{2}} = \left([I] + \sum_{k=1}^{F-2} \left([A]^{-1}[B] \right)^k \right) \varepsilon \Delta t_c \omega_{pj}^2 [A]^{-1} \cdot$$

$$\begin{bmatrix} E_x \\ E_y \\ E_z \end{bmatrix}^n + \left([A]^{-1} \cdot [B] \right)^{F-1} \cdot \begin{bmatrix} J_x \\ J_y \\ J_z \end{bmatrix}^{n-\frac{1}{2}} \quad (4)$$

where $F = \Delta t / \Delta t_c$ [F is used here instead of M as in [23] to avoid confusion with M in (3a) and (3)], ω_{pj} is the angular plasma frequency, $[I]$ is an identity matrix of size 3×3, and $[A]$ and $[B]$ are 3×3 matrices, which are defined in [5, Appendix].

The following two-parameter exponential ionosphere profile is used for the D-region of the ionosphere:

$$n_e(i, j, r) = 1.43 \times 10^{13}$$
$$* e^{(-0.15 * h'(i,j))} e^{((\beta(i,j) - 0.15) * (h - h'(i,j)))} \quad (5)$$

where n_e is the electron density in electrons/cm^3, h is the height (altitude) of the grid cell in km, h' (in km) controls the overall altitude of the profile, and the sharpness of the gradient is controlled by β in km^{-1}. This ionosphere profile originates from [8] and has been used with success in previous comparisons with theory and measurements [26], [27]. It also agrees with observed D-region profiles [28].

The plasma frequency has the following form [29]:

$$\omega_p(i, j, r) = 56.3803 * \sqrt{n_e(i, j, r)}. \quad (6)$$

The following electron–neutral collision frequency profile from [8] is used, which was found to closely match laboratory measurements [30], partial reflection data [31], and propagation-based rocket measurements [32]:

$$v_j(r) = 1.816 \times 10^{11} * e^{(-0.15 * h)} \quad (7)$$

where v_j is the collisional frequency.

All simulations in this article use a background magnetic field of 50 μT aligned in the vertical (radial) direction. Although the 3-D model may account for arbitrary directions and variations in the background magnetic field, the reason for assuming a vertical geomagnetic field is to avoid any possibility of the PML exhibiting an instability, see [33], [34]. The 2-D azimuthally symmetric FDTD model may only effectively simulate a vertical background magnetic field, since any incline to the geomagnetic field in that model would become azimuthally symmetric. Unfortunately, this is a restrictive assumption at VLF [15].

B. SIBC Ground Approximation

The wavelength at VLF is on the order of 10 m in the conductive oceans and 650 m in dry soil. As a result, for long propagation paths it is computationally infeasible to extend the FDTD model into the ground/oceans, since the FDTD model requires at least ten grid cells per wavelength. Instead, a surface impedance boundary condition (SIBC) is used along the Earth's surface. The SIBC method of [35] is used.

When the ground is not assumed to be a perfect electric conductor (PEC), ground conductivity, σ, and relative permittivity, ε_r, values currently existing in LWPC [36] for the propagation path of interest are implemented in the FDTD model.

C. CPML Boundary Conditions

The VLF signal will mostly be reflected or absorbed by the time it reaches the upper grid boundary (at 110 km). A ten-cell thick convolutional perfectly matched layer (CPML) [37], [38] absorbing boundary condition is implemented along the top of the FDTD grid to absorb any remaining VLF energy.

In the horizontal (w–e and s–n) directions, CPML is not used due to the known instability of PML in magnetized plasma for orientations of the background geomagnetic field not aligned in the direction of the PML [33]. Therefore, the computational domain is defined to be sufficiently large in the horizontal directions to prevent unwanted reflections from the domain edges over the time span of interest.

III. 2000 km PROPAGATION MODELING DETAILS

To obtain results over a 2000 km propagation path, the regional 3-D FDTD grid is constructed to span 4800 km along the propagation path (i-direction, aligned along the equator of the global model) and 2500 km in the horizontal direction perpendicular to the propagation path (j-direction, corresponding to the s–n direction of the global model). The model also extends vertically (radially, in the k-direction) from the sea level to an altitude of 110 km. The total number of grid cells in the i-, j-, and k-directions are 9600, 5040, and 309, respectively.

The grid resolution is 500 m in the horizontal directions (w–e and south–north directions). The resolution in the vertical direction is 500 m at the surface of the Earth, which increases to 250 m at an altitude of 67.5 km in order to account for the reduced electromagnetic wavelength in the ionosphere.

The VLF transmitter in Cutler, ME, USA, with a call sign of NAA is assumed to be the source. It operates at 24 kHz and radiates up to ∼1.8 MW of power. The NAA transmitter is modeled as a vertical (radial) current source along a single (500 m long) electric field component just above the Earth's surface

$$E_z^n(i_{source}, j_{source}, 1) = \sin(2\pi f(n - n_0)\Delta t) \cdot e^{-\left(\frac{n-n_0}{n_{half}}\right)^2} \quad (8)$$

where n is the time step number, $f = 24$ kHz, $\Delta t = 5$ ns, $n_0 = 240\ 000$ (1.2 s), and $n_{half} = 80\ 000$ (0.4 ms), resulting in a bandwidth of ∼1.590 Hz. The source is positioned at grid cell index $i_{source} = 2750$ and $j_{source} = 2520$. The time waveform is assumed to be a Gaussian modulating a sinusoid so that at the end of the simulation the field components may be allowed to decay to 0 over the propagation path of interest, and a DFT may be used to obtain the magnitude and phase at 24 kHz along the full propagation path. To avoid overly large output files, an on-the-fly DFT [13] is performed during time stepping.

A. Dispersion Error Corrections

Due to the long propagation paths being considered, numerical dispersion errors should be corrected. To account for this, after the DFT is performed on the field component time waveforms along the propagation path, the corrected phase is calculated using a basic Richardson extrapolation [39]

$$\phi_{corrected}(f, x) = \phi_{FDTD}(f, x, \Delta x) + K_f(f, x)x\Delta x^2 \quad (9)$$

where f is the source frequency in kHz, x is the distance from the source in km, ϕ_{FDTD} is the phase predicted by the FDTD model, Δx is the grid resolution along the propagation direction, and K_f is a dispersion constant that is frequency dependent. For the 2000 km propagation path of interest here, the K_f calculated in [18] is utilized

$$K_f = 0.001366 f^2 - 0.02611 f + 0.1540. \quad (10)$$

B. Computational Requirements

The regional 3-D FDTD model is comprised of a total of ~15 billion grid cells. It is parallelized onto a supercomputer using message passing interface (MPI) and runs on 28 800 processors. To allow the VLF waves to fully propagate over the propagation path of interest and also decay to 0, each simulation is run for a total of 2 million time steps, with $\Delta t = 5$ ns and $\Delta t_c = \Delta t/100$ [23]. Each simulation takes ~45 h in real time, and each of these simulations is divided into two or more segments using restart. Each simulation used ~3.9 TB memory, which includes for example all the field components, coefficients, and arrays for communicating between processors. Some of the SIBC and plasma coefficients are calculated with double precision.

IV. 2-D FDTD AND LWPC FOR COMPARISON

The 3-D FDTD model results are compared with a 2-D azimuthally symmetric FDTD model and LWPC results. For LWPC, the propagation path parameters were manually segmented every 20 km. The 2-D and 3-D FDTD models use different approaches for modeling the magnetized ionospheric plasma; however, the overall solutions for the algorithms are equivalent. The 2-D FDTD used here was developed in [19] and [20]. All three models assume the same ground profiles, ionosphere profiles, and background magnetic field. One primary difference between the FDTD models is that the 2-D model is run at double precision and the 3-D model is run at single precision (to keep the computational requirements more reasonable). There are no apparent differences introduced by running the models at double versus single precision for the propagation paths studied in this article.

V. 2000 km PROPAGATION RESULTS

A. PEC Ground With Homogenous Ionosphere Plasma

The first propagation scenario has a PEC ground with a homogenous daytime ionosphere, where $h' = 75$ km and $\beta = 0.5$ km^{-1}. In Fig. 2(a) and (b), the 3-D FDTD results are compared with those obtained from the LWPC and 2-D azimuthally symmetric FDTD models. The insets
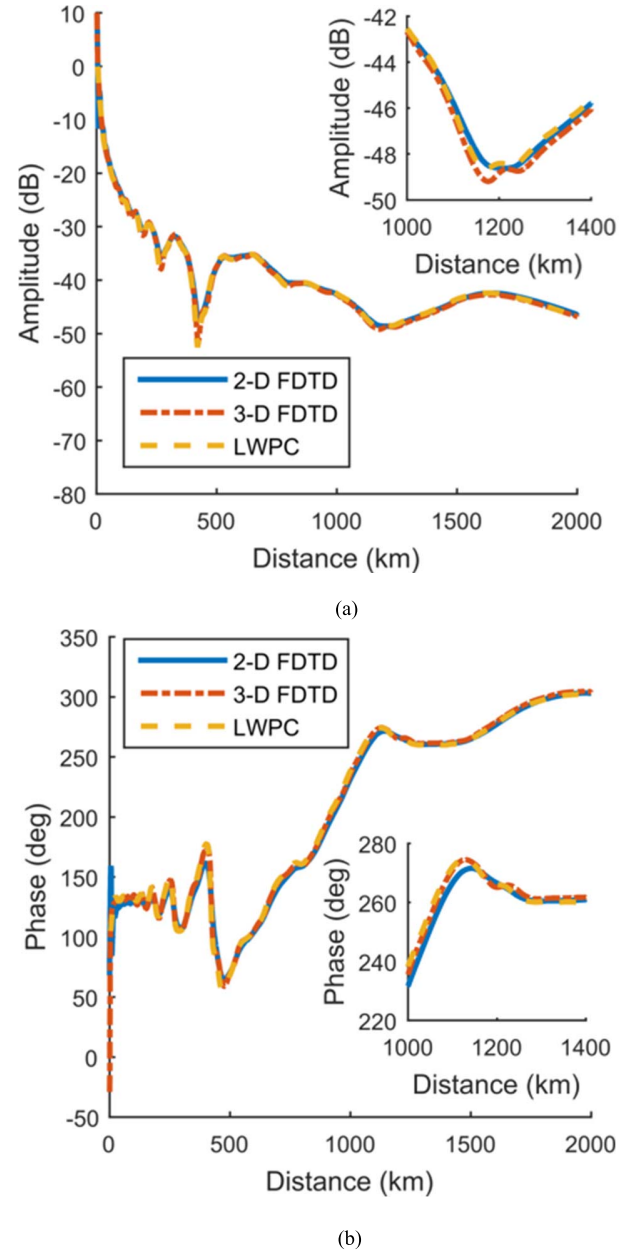

Fig. 2. (a) Amplitude and (b) phase variation versus distance from the NAA transmitter for a propagation path having homogeneous daytime ionospheric conditions and a perfectly electric conducting ground. Insets: Zoomed-in views of the results from 1000 to 1400 km.

of Fig. 2 show zoomed-in views of the results from 1000 to 1400 km.

The second propagation scenario has a PEC ground with a homogeneous nighttime ionosphere, where $h' = 85$ km and $\beta = 0.7$ km^{-1}. Fig. 3(a) and (b) shows the comparison of the 3-D FDTD results with those obtained from the LWPC and 2-D azimuthally symmetric FDTD models.

There is a very good agreement between the three models in Figs. 2 and 3. For the nighttime propagation path, there is a 360° phase change in Fig. 3(b) at ~400 km in the 3-D FDTD results relative to the 2-D FDTD and LWPC results. This phase shift is likely due to the depth of the null in the amplitude profile of Fig. 3(a) at the same location.
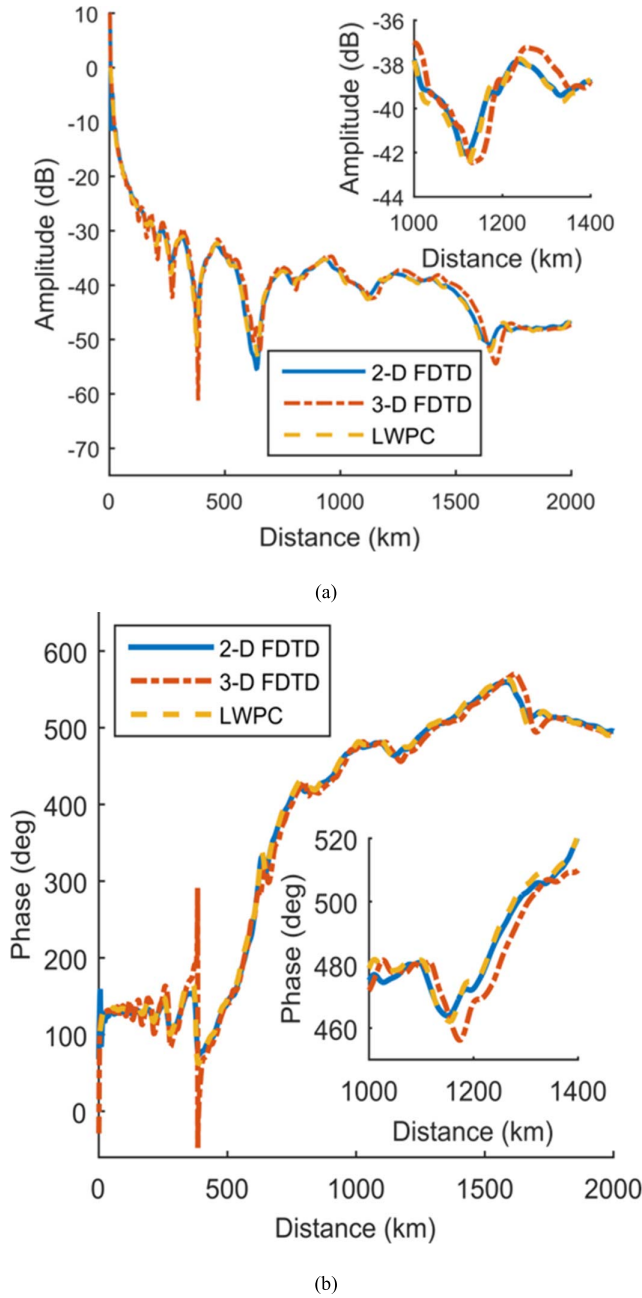
(a)

(b)

Fig. 3. Same as for Fig. 2, but for homogeneous nighttime ionospheric conditions. Insets: Zoomed-in views of the results from 1000 to 1400 km.

To provide a more quantitative comparison of the models, the 2-D and 3-D FDTD model results are compared against the LWPC result using a root-mean-squared error (RMSE) analysis. In this case, the LWPC data serves as a reference (not necessarily the correct) value along the propagation path. The following formula is used:

$$RMSE = \sqrt{\frac{\sum_{i=1}^{N}(\hat{y}_{iLWPC} - y_{i3D})^2}{N}}. \qquad (11)$$

The sum is taken over the distance from the source, and y_{i3D} and $\hat{y}_{iLWPC}$ represent either the amplitude or phase value observed at the indexed distance. Since the LWPC data are at a much coarser resolution than the FDTD data, the FDTD data are compared within a range of ± 5 km around each

LWPC data point. This method provides a means of evaluating the average difference between both methods over the entire 2000 km propagation path, where a smaller number represents a better agreement of the FDTD data with the reference LWPC data.

The 3-D FDTD data in Fig. 2 have an amplitude RMSE of 0.385 dB and a phase RMSE of 2.05°. This agreement is slightly stronger than the 2-D FDTD model that has RMSE values of 0.594 dB and 4.31° for the amplitude and phase, respectively.

The 3-D FDTD data in Fig. 3 have an amplitude RMSE of 1.54 dB and a phase RMSE of 18.1°. The larger phase value reflects both the spike at 380 km and the dispersion differences after 1000 km. This shows a very good relative agreement, but it is not as strong as the daytime result; and it is weaker than the 2-D FDTD RMSE of 0.768 dB and 4.75°, respectively.
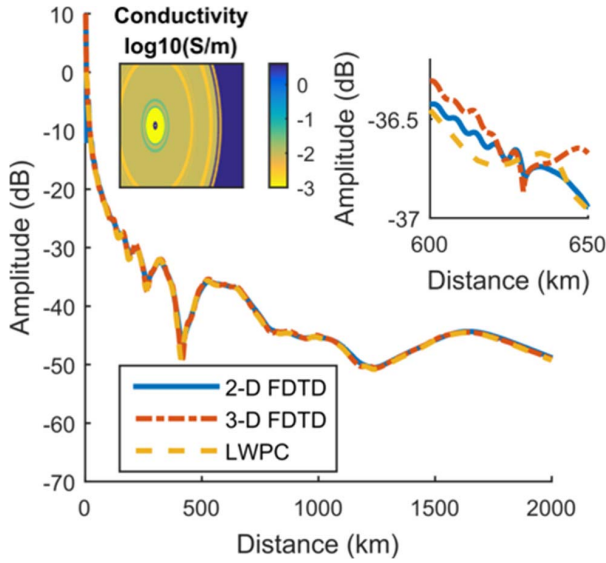
B. Realistic Ground With Azimuthal Symmetry and Homogeneous Ionosphere Plasma

Fig. 4 repeats the simulation of Fig. 2 but instead of assuming a PEC ground, a realistic ground is modeled using an SIBC. The ground profile along a propagation path from the NAA VLF transmitter in Cutler, ME toward New Mexico is assumed. Note that in this case, the ground profile in the 3-D model is assumed to be azimuthally symmetric in order to match the 2-D azimuthally symmetric FDTD modeling capabilities. Again, there is very good agreement between the three modeling approaches in Fig. 4. The 3-D FDTD amplitude data have an RMSE of 0.4115 dB, and the phase RMSE of 1.72°. This result indicates the impact of the ground relative to the result in Fig. 2. The 2-D FDTD model shows a very similar but slightly weaker agreement with an amplitude RMSE of 0.455 dB and phase RMSE of 2.80°.

The insets of Fig. 4 show the zoomed-in views of the amplitudes and phases along the propagation path from ∼600 to 650 km. The amplitude results in the inset of Fig. 4(a) demonstrate that both the 2-D and 3-D FDTD models account for perturbations caused by ground conductivity changes. Specifically, the amplitude oscillations in the FDTD results are generated from scattering and reflection from the ground conductivity change of 0.001 to 0.03 at a distance of 630 km. On the other hand, the abrupt ground conductivity change is not observable in the LWPC results. This is partly because in LWPC the propagation path is divided into 20 km long discrete slabs, so the ground conductivity change may not be occurring exactly at the location at which it is accounted for in the 500 m resolution FDTD models. Another reason the ground conductivity change is not observable in the LWPC model is because LWPC does not account for scattering or reflection.

C. Realistic Ground and Daytime-to-Nighttime Ionosphere Gradient With Azimuthal Symmetry

Fig. 5 repeats the simulation of Fig. 4, but with the ionosphere changed to a linear gradient varying from daytime-to-nighttime conditions along the propagation path. Sunrise and sunset effects on VLF propagation have been of interest for many decades see [40], [41]. In this case, the 3-D model

(a)
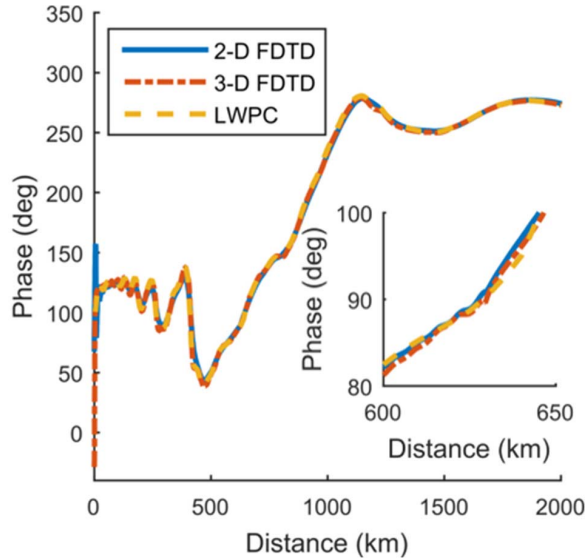
(b)

Fig. 4. Same as for Fig. 2, but with realistic ground conditions from the NAA transmitter toward New Mexico modeled with azimuthal symmetry using an SIBC. Insets: Zoomed-in views of the amplitudes and phases at distances of ~600 to 650 km from the transmitter. (a) also includes an inset showing the assumed ground conductivity with azimuthal symmetry.

assumes both the ground and ionosphere are azimuthally symmetric around the source as indicated by the inset. The results again show good agreement between the three models. Specifically, the 3-D FDTD amplitude has an RMSE of 0.495 dB and the phase RMSE of 2.96°. Comparing these numbers with those from Section V-B (Fig. 4), highlights the impact of the gradient ionosphere. The 2-D RMSE values are nearly the same as the 3-D FDTD values, with the 2-D model having an RMSE amplitude of 0.511 dB and a phase RMSE of 3.378°.

D. Fully 3-D Daytime-to-Nighttime Transition Oriented Along the Propagation Path

Fig. 6 first lists the comparison of the azimuthally symmetric 2-D FDTD results of Fig. 5 with an analogous 2-D
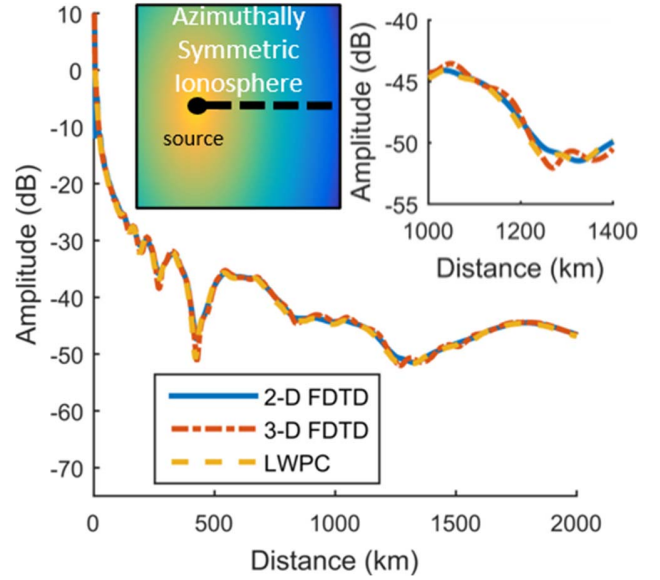
(a)
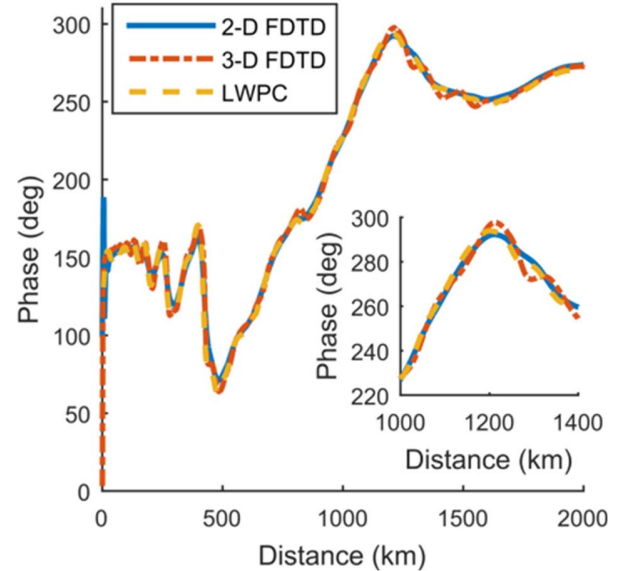
(b)

Fig. 5. (a) Amplitude and (b) phase variation versus distance from the NAA transmitter for a propagation path having a linear gradient ionosphere changing from daytime to nighttime along the propagation path (as shown in the inset, where the color scheme corresponds to the height of the ionosphere; yellow corresponds to day and dark blue corresponds to night). The 3-D model assumes the ground and ionosphere conditions are cylindrically symmetric around the source as indicated by the inset. The black dot in the inset shows the location of the transmitter. The black dashed line shows the propagation path of interest. The other pair of insets show zoomed-in views of the results from 1000 to 1400 km.

simulation with the ground conditions changed from the NAA to NM path instead of a homogeneous ocean surface. The differences between these two 2-D results highlight the impact of the ground parameters on the propagation results.

In addition, Fig. 6 shows the comparison of results for an ocean surface propagation path with (1) an azimuthally symmetric linear gradient daytime-to-nighttime ionosphere in the 2-D FDTD model and (2) a fully 3-D linear gradient
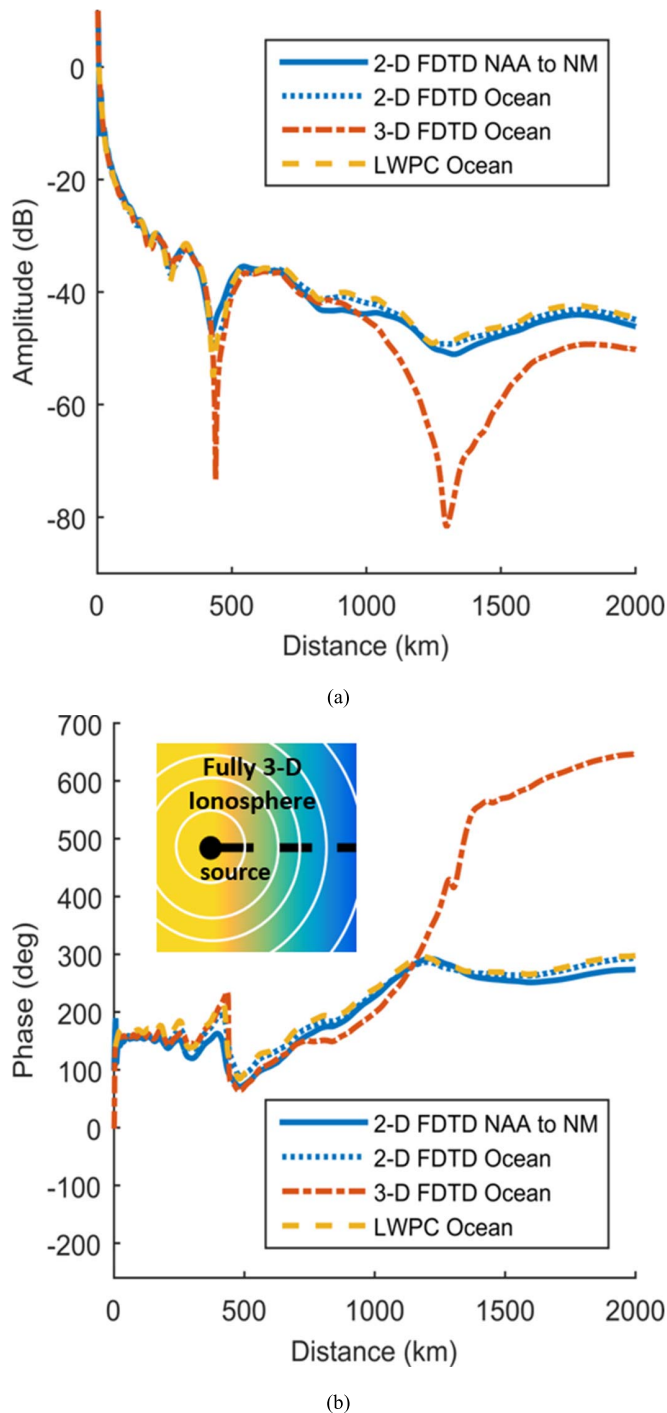
(a)

(b)

Fig. 6. Same as for Fig. 5, but the two 2-D model results show the differences introduced by a realistic ground from the NAA transmitter toward NM versus an ocean surface. The 3-D model assumes that the ocean surface and the ionosphere are fully 3-D. In the inset, the black dot shows the location of the transmitter. The black dashed line in the inset shows the propagation path of interest. The colors depict the ionospheric conditions in the 3-D model. Yellow corresponds to day and dark blue corresponds to night. The white lines are contour lines of the azimuthally symmetric day-to-night ionsopheric profile used in the 2-D azimuthally symmetric model.

daytime-to-nighttime ionosphere in the 3-D model. The orientation of the fully 3-D linear gradient ionosphere is shown in the inset, which plots the height of the ionosphere changing from daytime conditions (yellow) at the source to nighttime conditions (dark blue) at a distance of 2000 km.
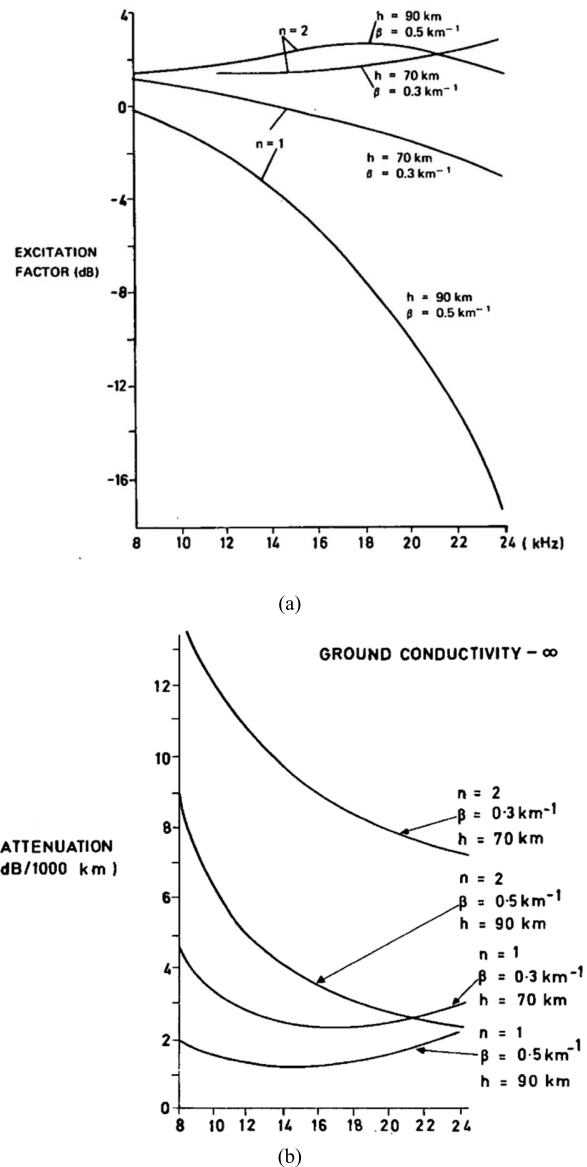

(a)

(b)

Fig. 7. (a) Plot of the excitation factor for modes TM_1 and TM_2 at different VLF frequencies for day and night conditions (Courtesy of [8]). The parameter β is the same as defined in (6), h corresponds to h' in (6), and n corresponds to the mode number. (b) Plot of attenuation rates of TM_1 and TM_2 modes for day and night conditions (Courtesy of [8]).

There are noticeable differences between the 2-D azimuthally symmetric and fully 3-D linear gradient ionosphere results, particularly for distances beyond 1000 km. Most notably, the 2-D model does not predict the null at ∼1300 km because it assumes a different (incorrect) azimuthally symmetric ionosphere. The reason for these differences is explained as follows. At 24 kHz, the second transverse magnetic mode (TM_2) is excited at the transmitter more easily than the first transverse magnetic mode (TM_1), as is shown in Fig. 7(a) [8]. Then, the TM_1 and TM_2 modes attenuate at different rates during day versus night as shown in Fig. 7(b). When sunset occurs along the propagation path, there is effectively a discontinuity in the height of the waveguide. The height discontinuity changes gradually during the transition from day to night. Mode conversions occur at such a discontinuity [42].
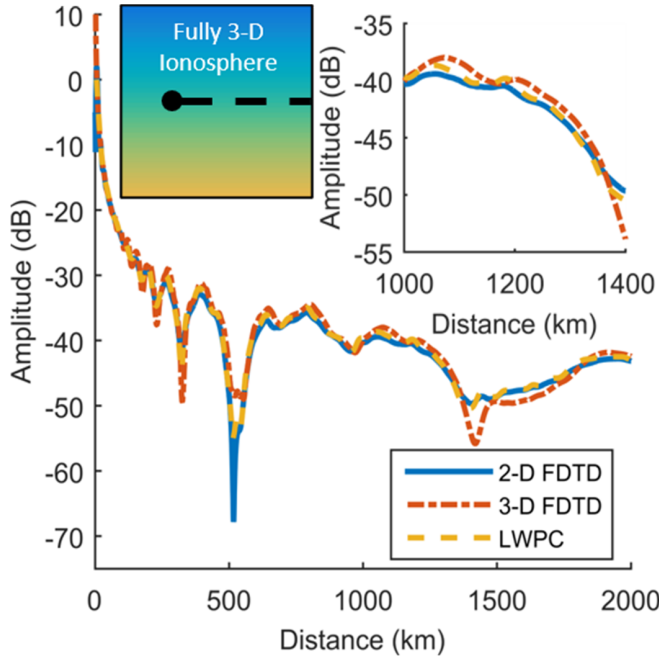
(a)
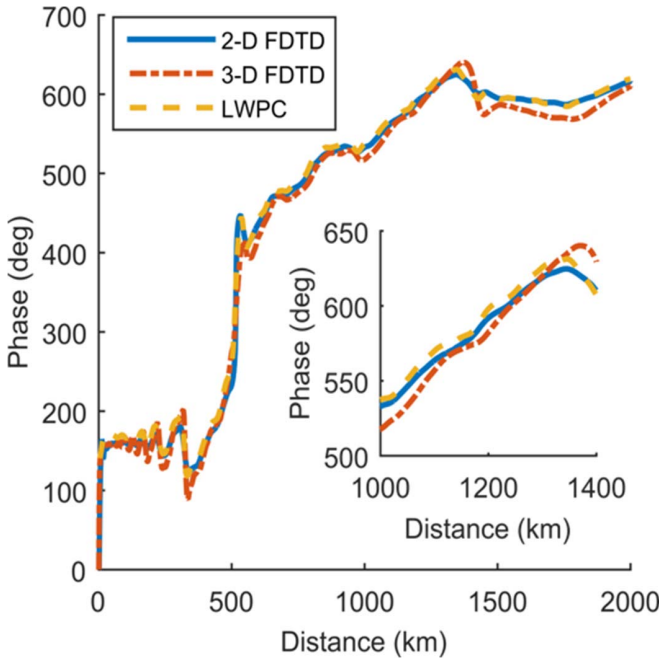
(b)

Fig. 8. Analogous to the ocean surface results of Fig. 6, but with the ionosphere linear gradient perpendicular to the propagation path. In the inset on the left, the black dot shows the location of the transmitter, and the black dashed line shows the propagation path of interest. Yellow corresponds to day and dark blue corresponds to night. The other insets show zoomed-in views of the results from 1000 to 1400 km.

As a result, the differences in the propagation results of the 3-D model versus the 2-D model indicate that the effective height of the waveguide along the propagation path is slightly different for an azimuthally symmetric day-to-night transition versus a fully 3-D day-to-night transition. This impacts the conversion of modes along the propagation path as well as the

attenuate rates of the different modes as the waveguide height changes. All this introduces a different interference pattern in the 3-D model and leads to the additional null at 1300 km that is not seen in the 2-D model. To a lesser degree, since it occurs earlier along the propagation path and the day-to-night transition, the null at ~450 km caused by interference between the propagating modes is also impacted.

In summary, the null at ~1300 km is not a numerical artifact. The existence of that null indicates that a fully 3-D FDTD model is important to properly account for the mode conversion and the subsequent interaction between the different propagating modes when there is a day-to-night transition along the propagation path. The benefits of a fully 3-D model are most pronounced after distances of ~1000 km when sunset begins near the transmitter (after the halfway point of the transition from day to night). Thus, if the day-to-night transition were to begin further away from the transmitter, it is expected that the fully 3-D model would be most beneficial at and beyond where the half-way point between the day-to-night transition is located.

E. Fully 3-D Daytime-to-Nighttime Ionosphere Transition Oriented Perpendicularly to the Propagation Path

Fig. 8 shows results for an ocean surface, as in Fig. 6, but with the ionosphere linear day-to-night transition now oriented perpendicular to the direction of propagation. The 2-D FDTD model is unable to account for a gradient perpendicular to the direction of propagation. As a result, that model assumes a homogeneous ionosphere set to the midpoint of the daytime-to-nighttime ionosphere gradient. On the other hand, the fully 3-D model includes all the features of the daytime-to-nighttime ionosphere gradient.

Fig. 8 shows the comparison of the 2-D and fully 3-D FDTD results along the propagation path. Most notably, the agreement is not as close beyond the first ~400 km as it was in Fig. 5. Using the results in Fig. 6, this lack of agreement is due to the 2-D azimuthally symmetric FDTD model not being able to fully account for the fully 3-D ionosphere along the entire propagation path. On the other hand, the overall behavioral similarities between the 2-D and 3-D results are attributed to the fact that the effective height of the waveguide is identical along the propagation path in both the 2-D homogeneous model and the fully 3-D model when there is an ionospheric day-to-night transition oriented perpendicularly to and centered on the propagation path.

VI. CONCLUSION

This work presents the 3-D FDTD modeling results for VLF propagation over 1000 km-scale distances in the Earth-ionosphere waveguide. These 3-D simulations were very computationally demanding, requiring for each simulation 28 800 processing cores for over 45 h and ~3.9 TB memory. Hence, it is important to know under what conditions 2-D azimuthally symmetric FDTD and LWPC models provide sufficiently accurate results versus when a fully 3-D model is needed.

	LWPC	2-D FDTD	3-D FDTD
Computation time	Fastest (~10 Seconds)	Medium (~6 hours on a 12-core processor)	Slowest (~45 hours on 28,800 Processors)
Physical Geometries that may be directly modeled	2-D homogeneous Waveguide Segments	2-D Azimuthally-Symmetric Geometries	Fully 3-D (Usually Homogeneous within each 3-D Grid Cell)
Relative Accuracy for Day-to-Night Transitions Parallel to the Propagation Path	Good Until the midpoint of the day-to-night transition	Good Until the midpoint of the day-to-night transition	Good over the Full Propagation Path
Relative Accuracy for Day-To-Night Transitions Perpendicular to the Propagation Path	Mostly good for a propagation path within the day-night transition zone when the 3-D ionospheric conditions are spatially averaged to those along the propagation path	Mostly good for a propagation path within the day-night transition zone when the 3-D ionospheric conditions are spatially averaged to those along the propagation path	Good over the Full propagation Path

The calculated amplitude and phase results versus distance from a VLF transmitter operating at 24 kHz showed that the 2-D azimuthally symmetric FDTD models agree well with the 3-D model for homogeneous ionospheric and ground conditions, and for azimuthally symmetric geometries. The 2-D FDTD model also provides comparable results until the midpoint of a daytime-to-nighttime transition for the case of a daytime-to-nighttime transition oriented parallel to the direction of propagation. Beyond the midpoint between day and night, the 2-D FDTD model deviates drastically from the 3-D model and misses a null at 300 km beyond the midpoint due to differences in the mode conversion between the two models. Finally, for the case of a linear ionosphere gradient oriented perpendicular to the propagation path, the predicted magnitude and phase of the 2-D and 3-D FDTD models along the propagation path are closer than for the parallel gradient (they both follow a similar pattern), due to the fact that the effective height of the waveguide is identical between the two models along the direction of propagation. The deviations between the two models arise from the inability of the 2-D FDTD model to account for the fully 3-D geometry and propagation. Table I summarizes all these findings and also provides an overall comparison of three models.

Future work will include the modeling of localized ionospheric perturbations along and near the propagation path in the 3-D FDTD model for comparison with comparable 2-D FDTD and LWPC models. Furthermore, the impact of nonvertical and spatially varying background magnetic fields on the propagation characteristics should be studied. Distribution Statement A. Approved for public release: distribution unlimited.

ACKNOWLEDGMENT

REFERENCES

[1] A. D. Watt and R. D. Croghan, "Comparison of observed VLF attenuation rates and excitation factors with theory," *Radio Sci. J. Res. NBS/USNC-URSI*, vol. 68D, no. 1, pp. 1–9, 1964.

[2] U. S. Inan, S. A. Cummer, and R. A. Marshall, "A survey of ELF and VLF research on lightning-ionosphere interactions and causative discharges," *J. Geophys. Res., Space Phys.*, vol. 115, no. A6, pp. 1–21, Jun. 2010, doi: 10.1029/2009JA014775.

[3] R. D. Hansucker and J. K. Hargreaves, *The High-Latitude Ionosphere and Its Effects on Radio Propagation*. Cambridge, U.K.: Cambridge Univ. Press, 2002.

[4] M. B. Cohen, U. S. Inan, R. K. Said, and T. Gjestland, "Geolocation of terrestrial gamma-ray flash source lightning," *Geophys. Res. Lett.*, vol. 37, no. 2, Jan. 2010, Art. no. L02801, doi: 10.1029/2009GL041753.

[5] G. Bainbridge and U. S. Inan, "Ionospheric D region electron density profiles derived from the measured interference pattern of VLF waveguides," *Radio Sci.*, vol. 38, no. 4, p. 1077, 2003. [Online]. Available: https://agupubs.onlinelibrary.wiley.com/doi/pdf/10.1029/2002RS002686

[6] R. Turner, "Submarine communication antenna systems," *Proc. IRE*, vol. 47, no. 5, pp. 736–739, 1959.

[7] K. G. Budden, *The Wave-Guide Mode Theory of Wave Propagation*. London, U.K.: Logos Press, 1961.

[8] J. R. Wait and K. P. Spies, "Characteristics of the earth-ionosphere waveguide for VLF radio waves," Nat. Bur. Standards, Gaithersburg, MD, USA, Tech. Note 300, Dec. 1964.

[9] P. B. Morris, R. R. Gupta, R. S. Warren, and P. M. Creamer, "OMEGA navigation system course book," USD Transp., TASC, Reading, MA, USA, Tech. Rep. 2-D-5, 1994.

[10] J. A. Ferguson and F. P. Snyder, "The segmented waveguide for long wavelength propagation calculations," Nav. Ocean Syst. Center, San Diego, CA, USA, Tech. Rep. 1071, 1986.

[11] K. Baba and M. Hayakawa, "The effect of localized ionospheric perturbations on subionospheric VLF propagation on the basis of finite element method," *Radio Sci.*, vol. 30, no. 5, pp. 1511–1517, Sep. 1995.

[12] K. Yee, "Numerical solution of initial boundary value problems involving Maxwell's equations in isotropic media," *IEEE Trans. Antennas Propag.*, vol. AP-14, no. 3, pp. 302–307, May 1966. [Online]. Available: https://ieeexplore.ieee.org/document/1138693

[13] A. Taflove and S. C. Hagness, *Computational Electromagnetics: The Finite-Difference Time-Domain Method*, 3rd ed. Norwood, MA, USA: Artech House, 2005.

[14] M. Thevenot, J.-P. Berenger, T. Monediere, and F. Jecko, "A FDTD scheme for the computation of VLF-LF propagation in the anisotropic earth-ionosphere waveguide," *Annales Telecommun.*, vol. 54, nos. 5–6, pp. 297–310, 1999.

[15] S. A. Cummer, "Modeling electromagnetic propagation in the earth-ionosphere waveguide," *IEEE Trans. Antennas Propag.*, vol. 48, no. 9, pp. 1420–1430, Sep. 2000.

[16] S. A. Cummer and J. Li, "Accurate modeling of ionospheric electromagnetic fields generated by a low altitude VLF transmitter," Air Froce Res. Lab., Wright-Patterson Air Force Base, OH, USA, Sci. Rep. 2, 2009.

[17] J.-P. Berenger, "Long range propagation of lightning pulses using the FDTD method," *IEEE Trans. Electromagn. Compat.*, vol. 47, no. 4, pp. 1008–1011, Nov. 2005.

[18] R. A. Marshall, T. Wallace, and M. Turbe, "Finite-difference modeling of very-low-frequency propagation in the earth-ionosphere waveguide," *IEEE Trans. Antennas Propag.*, vol. 65, no. 12, pp. 7185–7197, Dec. 2017.

[19] R. A. Marshall, "An improved model of the lightning electromagnetic field interaction with the D-region ionosphere," *J. Geophys. Res., Space Phys.*, vol. 117, no. A3, Mar. 2012, Art. no. A03316.

[20] R. A. Marshall, "Effect of self-absorption on attenuation of lightning and transmitter signals in the lower ionosphere," *J. Geophys. Res., Space Phys.*, vol. 119, no. 5, pp. 4062–4076, May 2014, doi: 10.1002/2014ja019921.

[21] J. J. Simpson and A. Taflove, "Three-dimensional FDTD modeling of impulsive ELF propagation about the earth-sphere," *IEEE Trans. Antennas Propag.*, vol. 52, no. 2, pp. 443–451, Feb. 2004, doi: 10.1109/TAP.2004.823953.

[22] A. Samimi and J. J. Simpson, "Parallelization of 3-D global FDTD Earth-ionosphere waveguide models at resolutions on the order of ~1 km and higher," *IEEE Antennas Wireless Propag. Lett.*, vol. 15, pp. 1959–1962, 2016. [Online]. Available: https://my.ece.utah.edu/~simpson/Papers/Paper29.pdf

[23] S. Pokhrel, V. Shankar, and J. J. Simpson, "3-D FDTD modeling of electromagnetic wave propagation in magnetized plasma requiring singular updates to the current density equation," *IEEE Trans. Antennas Propag.*, vol. 66, no. 9, pp. 4772–4781, Sep. 2018, doi: 10.1109/tap.2018.2847601.

[24] Y. Yu and J. J. Simpson, "An E-J collocated 3-D FDTD model of electromagnetic wave propagation in magnetized cold plasma," *IEEE Trans. Antennas Propag.*, vol. 58, no. 2, pp. 469–478, Feb. 2010, doi: 10.1109/tap.2009.2037706.

[25] A. Samimi and J. J. Simpson, "An efficient 3-D FDTD model of electromagnetic wave propagation in magnetized plasma," *IEEE Trans. Antennas Propag.*, vol. 63, no. 1, pp. 269–279, Jan. 2015, doi: 10.1109/tap.2014.2366203.

[26] J. E. Bickel, J. A. Ferguson, and G. V. Stanley, "Experimental observation of magnetic field effects on VLF propagation at night," *Radio Sci.*, vol. 5, no. 1, p. 19, 1970.

[27] N. R. Thomson, "Experimental daytime VLF ionospheric parameters," *J. Atmos. Terr. Phys.*, vol. 55, p. 173, Feb. 1993.

[28] C. F. J. Sechrist, "Comparisons of techniques for measurement of D-region electron densities," *Radio Sci.*, vol. 9, no. 2, p. 137, 1974.

[29] K. G. Budden, *The Propagation of Radio Waves*. Cambridge, U.K.: Cambridge Univ. Press, 1985.

[30] A. V. Phelps and J. L. Pack, "Electron collision frequencies in nitrogen and in the lower ionosphere," *Phys. Rev. Lett.*, vol. 3, no. 7, p. 340, 1959.

[31] J. S. Belrose and M. J. Burke, "Study of the lower ionosphere using partial reflection I: Experimental technique and method of analysis," *J. Geoph. Res.*, vol. 69, no. 13, p. 2799, 1964.

[32] J. A. Kane, "Re-evaluation of ionospheric electron densities and collision frequencies derived from rocket measurements of refractive index and attenuation," *J. Atmos. Terr. Phys.*, vol. 23, p. 338, Dec. 1962.

[33] M. W. Chevalier, T. W. Chevalier, and U. S. Inan, "A PML utilizing k-vector information as applied to the whistler mode in a magnetized plasma," *IEEE Trans. Antennas Propag.*, vol. 54, no. 8, pp. 2424–2429, Aug. 2006.

[34] W. Hu and Cummer, "The nearly perfectly matched layer is a perfectly matched layer," *IEEE Antennas Wireless Propag. Lett.*, vol. 3, pp. 137–140, 2004.

[35] K. S. Oh and J. E. Schutt-Aine, "An efficient implementation of surface impedance boundary conditions for the finite-difference time-domain method," *IEEE Trans. Antennas Propag.*, vol. 43, no. 7, pp. 660–666, Jul. 1995.

[36] J. A. Ferguson, "Computer programs for assessment of long-wavelength radio communications, version 2.0, user's guide and source files," Space Naval Warfar Syst. Center, Charleston, SC, USA, Tech. Document 3030, May 1998.

[37] J. P. Berenger, "A perfectly matched layer for the absorption of the electromagnetic waves," *J. Comput. Phys.*, vol. 114, no. 2, pp. 185–200, 1994.

[38] J. A. Roden and S. D. Gedney, "Convolution PML (CPML): An efficient FDTD implementation of the CFS-PML for arbitrary media," *Microw. Opt. Technol. Lett.*, vol. 27, no. 5, pp. 334–339, 2000.

[39] L. F. Richardson and J. A. Gaunt, "The deferred approach to the limit. Part I. Single lattice. Part II. Interpenetrating latices," *Philos. Trans. Roy. Soc. London A, Math. Phys. Sci.*, vol. 226, nos. 636–646, 1927, Art. no. 299361. [Online]. Available: http://rsta.royalsocietypublishing.org/content/226/636-646/299

[40] D. Walker, "Phase steps and amplitude fading of VLF signals at dawn and dusk," *Radio Sci. J. Res. NBS/USNC-URSI*, vol. 69D, no. 11, pp. 1435–1443, 1965.

[41] J. E. Samanes, J.-P. Raulin, E. L. Macotela, and W. R. G. Day, "Estimating the VLF modal interference distance using the South America VLF network (SAVNET)," *Radio Sci.*, vol. 50, no. 2, pp. 122–129, Feb. 2015, doi: 10.1002/2014rs005582.

[42] B. Burgess, "VLF phase delay variability and the design of long range navigation aids," in *Proc. AGARD Conf.*, no. 33, 1970, pp. 13–18.

Sean Burns (Student Member, IEEE) received the B.S. degree in mathematics and physics from The University of Utah, Salt Lake City, UT, USA, in 2013, where he is currently pursuing the Ph.D. degree in electrical and computer engineering.

His current research interests include finite-difference time-domain modeling of very-low-frequency radio waves in the Earth-ionosphere waveguide.

Forrest Gasdia received the B.S. and M.S. degrees in engineering physics from Embry–Riddle Aeronautical University, Daytona Beach, FL, USA, in 2014 and 2016, respectively. He is currently pursuing the Ph.D. degree in aerospace engineering sciences with the University of Colorado Boulder, Boulder, CO, USA.

His research interests include numerical modeling and statistical estimation of the lower ionosphere using very-low-frequency radio waves.

Jamesina J. Simpson (Senior Member, IEEE) received the B.S. and Ph.D. degrees in electrical engineering from Northwestern University, Evanston, IL, USA, in 2003 and 2007, respectively.

She is currently an Associate Professor with the Electrical and Computer Engineering Department, The University of Utah, Salt Lake City, UT, USA. Her research lab encompasses the application of the full-vector Maxwell's equations finite-difference time-domain (FDTD) method to electromagnetic wave propagation spanning 15 orders of magnitude across the electromagnetic spectrum. In particular, her group specializes in electromagnetic wave propagation within the global Earth-ionosphere waveguide.

Dr. Simpson received the 2010 National Science Foundation CAREER Award, the 2012 IEEE AP-S Donald G. Dudley, the Jr. Undergraduate Teaching Award, the 2017 URSI Santimay Basu Medal, and the 2020 IEEE AP-S Lot Shafai Mid-Career Distinguished Achievement Award.

Robert A. Marshall (Member, IEEE) received the B.S. degree in electrical engineering from the University of Southern California, Los Angeles, CA, USA, in 2002, and the M.S. and Ph.D. degrees in electrical engineering from Stanford University, Stanford, CA, USA, in 2004 and 2009, respectively.

He held various research positions at the Center for Space Physics, Boston University, Boston, MA, USA, and also at the Department of Aeronautics and Astronautics, Stanford University. He is currently an Assistant Professor with the Ann and H. J. Smead Department of Aerospace Engineering Sciences, University of Colorado Boulder, Boulder, CO, USA. He has authored the book *Numerical Electromagnetics: The FDTD Method* (Cambridge University Press, 2011) with U.S. Inan. His research interests include the study of lightning–ionosphere interactions, radiation belt precipitation and atmospheric effects, numerical modeling and applications in space physics, and small satellite instrument development.

Dr. Marshall was a recipient of the URSI Young Scientist Award in 2011.